Investigation of Spin-Wave Dynamics in Gyroid Nanostructures

Mateusz Gołębiewski,[1,*] Riccardo Hertel,[2] Vitaliy Vasyuchka,[3] Mathias Weiler,[3] Philipp Pirro,[3] Maciej Krawczyk,[1] Shunsuke Fukami,[4,5,6,7] Hideo Ohno,[4,5,6,7,8] and Justin Llandro[4,5]

[1] *Institute of Spintronics and Quantum Information, Faculty of Physics, Adam Mickiewicz University, Uniwersytetu Poznańskiego 2, 61-614 Poznań, Poland*
[2] *Université de Strasbourg, CNRS, Institut de Physique et Chimie des Matériaux de Strasbourg, F-67000 Strasbourg, France*
[3] *Fachbereich Physik and Landesforschungszentrum OPTIMAS, Rheinland-Pfälzische Technische Universität Kaiserslautern-Landau, Erwin-Schrödinger-Straße 56, 67663 Kaiserslautern, Germany*
[4] *Research Institute of Electrical Communication Information Devices Division Spintronics, Tohoku University, 2-1-1 Katahira, Aoba-ku, Sendai-shi, Miyagi 980-8577 Japan*
[5] *Center for Science and Innovation in Spintronics (CSIS), Tohoku University, Sendai 980-8577, Japan*
[6] *Center for Innovative Integrated Electronic Systems (CIES), Tohoku University, 468-1 Aramaki Aza Aoba, Aoba-ku, Sendai 980-0845 Japan*
[7] *WPI Advanced Institute for Materials Research, Tohoku University, 2-1-1 Katahira, Aoba-ku, Sendai 980-8577, Japan*
[8] *Inamori Research Institute for Science, Kyoto 600-8411, Japan*

(Dated: May 11, 2023)

A new concept in magnonics studies the dynamics of spin waves (SWs) in three-dimensional nanosystems. It is a natural evolution from conventionally used planar systems to explore magnetization configurations and dynamics in 3D nanostructures with lengths near intrinsic magnetic scales. In this work, we perform broadband ferromagnetic resonance (BBFMR) measurements and micromagnetic simulations of nanoscale magnetic gyroids – a periodic chiral structure consisting entirely of chiral triple junctions. Our results show unique properties of the network, such as the localization of the SW modes, evoking their topological properties, and the substantial sensitivity to the direction of the static magnetic field. The presented results open a wide range of applications in the emerging field of 3D magnonic crystals and spintronics.

I. INTRODUCTION

Spin waves (SWs) and their manipulation in magnetic materials encompass various topics in today's research community. In ferromagnets, SW dynamics are determined by the coexistence of magnetostatic and exchange interactions. In thin structures, the magnetostatic interactions are highly anisotropic and cause the SW properties to be strongly dependent on the relative orientation of the magnetization and the wavevector. This provides properties uncommon to other types of waves, such as negative group velocity, caustics, easily achievable nonlinearity, and dynamic reconfigurability control [1]. Among others, the technology of signal propagation without emission of Joule-Lenz heat [2–4], adjustable dispersion and group velocity [5–8] and the development of magnonic systems that are highly efficient and effective [2, 9–11], emphasize the unique properties of SWs and justify their extensive research [12, 13], the goal of which is to adapt the dynamics of magnetization in the high-tech industry.

Nanostructured 3D networks may give rise to topological and geometrical effects and emergent material properties, offering new possibilities for SW manipulation [14, 15]. There is considerable potential to explore the properties of such structures, for example by tuning their unit cell geometry and lattice period. A fully interconnected 3D system opens up a new degree of freedom for novel phenomena, allowing interactions and collective effects in all three dimensions [16–18]. In recent years, there has been a significant development of new fabrication techniques such as two-photon lithography, focused electron beam deposition, and block copolymer templating, which now allow the fabrication and measurement of complex 3D structures on the nanometer scale [19–23].

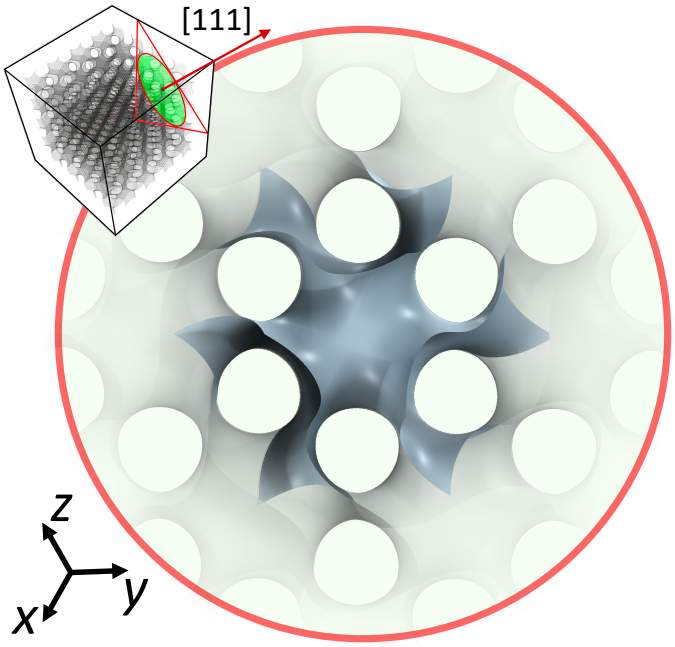

Figure 1. The gyroid surface model ($\phi = 0\%$) with the distinguished unit cell in the crystallographic direction [111] revealing the hexagonal distribution of the channels.

This paper analyzes a promising yet hardly explored structure in magnetism called a gyroid, which was discovered and first presented in 1970 [24]. It is defined by chiral

* mateusz.golebiewski@amu.edu.pl

triple junctions and periodicity in all three spatial directions, classified as $I4_132$ space group (No. 214) [25]. In recent years, many studies have been published describing gyroids in the field of photonics, where they have been presented as potential chiral beamsplitters [26], nonlinear optical metamaterials [27–29], or photonic crystals [30–34]. It has also inspired many research groups into the fabrication of artificial systems based on this geometry [26–28, 35–43]. The 3D structural units of nanoscale gyroids have both chirality and curvature, which has recently been shown to be highly effective for controlling non-collinear spin textures [44]. The effective Dzyaloshinskii-Moriya interaction and the curvature-related anisotropy are further important research in this context [45–48]. Curved magnetic wires and films also exhibit various mesmerizing effects [49], which together with chiral and topological properties [50, 51], open new avenues for future research. Thus, gyroids are an intriguing candidate for the realization of artificial 3D magnonic crystals with highly coupled geometric and magnetic states [52]. Furthermore, if gyroids are shown to adopt a significant number of energetically equivalent stable states, they become potential for artificial spin ice systems and active elements in unconventional computing architectures [53]. Recently, numerical and experimental visualization of the magnetic structure in a single and double $Ni_{75}Fe_{25}$ gyroid network has also been performed [19].

In our research, we analyze these structures from a magnonic point of view and measure, using broadband FMR, the collective dynamics of spin waves as a function of the orientation of the external magnetic field relative to the crystallographic axes of the gyroid. Using micromagnetic simulations, we show that the experimentally measured excitations are related to modes localized inside the structure, giving a new picture of the impact of nanoscale gyroid effects on macroscopic results. These studies show the strong influence of the gyroid morphology on the magnetization precession.

II. GEOMETRY AND MATERIAL PARAMETERS

As can be seen from Fig. 1, there are no straight lines or planar symmetries in the gyroid. In Ref. [54] the surface was given for the first time using conjugate surface construction, and in Ref. [55] its embedding was subsequently proved. The volume fractions of minimal and constant mean curvature gyroids have been further investigated numerically [56] with the constant mean curvature variants of the geometry.

In other fields, the gyroid is referred to as Laves' graph of girth ten [57] and the K_4 crystal [58, 59]. It consists of cubic unit cells composed of triple bonds connected by nanorods with elliptical cross sections for the non-zero volume filling fraction ϕ, the range of which is described in Ref. [28]. For $\phi = 0\%$ (see Fig. 1), a gyroid surface divides space into two labyrinths of paths oriented in opposite directions. The empty, unobstructed channels pass through the gyroid labyrinths in directions [100] and [111], and the paths emerge at 70.5 deg angles to any given channel as it passes through. Circling or gyrating down the channel in this way gives rise to the term "gyroid". Interestingly, gyroids exist in several Schwarz surface families that preserve different symmetries of triply periodic minimal surfaces and, like many others, can be approximated by a trigonometrical equation, in this case:

$$\begin{aligned} &\sin(2\pi x/L)\cos(2\pi y/L)+ \\ &\sin(2\pi y/L)\cos(2\pi z/L)+ \\ &\sin(2\pi z/L)\cos(2\pi x/L) \leq (101.5-2\phi)/68.1, \end{aligned} \tag{1}$$

where L is the gyroid's unit cell length.

A gyroid nanostructure was fabricated by thermally annealing a block copolymer template, selectively dissolving, and electrodepositing it, as described in Ref. [19]. The material used to fabricate the nanostructure is nickel (Ni), while the substrate is fluorine doped tin oxide-coated glass (FTO). The unit cell of the analyzed gyroid sample is 50 nm and $\phi \approx 10\%$. As a result, individual strut diameters are typically a few nanometers and therefore comparable to the intrinsic magnetic length scales, such as exchange length, domain wall width, and SW wavelength.

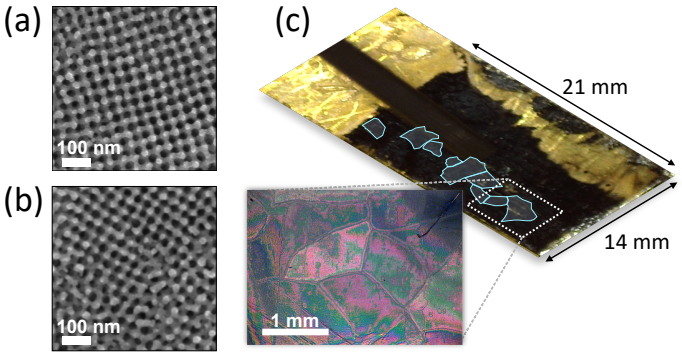

Figure 2. Multi-domain gyroid structure used in BBFMR measurements. In (a) and (b), scanning electron microscope images of two exemplary gyroid domains are shown – The difference between the two is manifested by their different crystallographic direction and amorphousness. In (c), a photograph of the entire sample is presented with the approximate location of several larger domains found by polarized light microscopy.

The sample used in the experiment has 12 unit cells per thickness, corresponding to 600 nm. Another important aspect of the measurements and the ferromagnetic response of the gyroid network is its orientation with respect to the static magnetic field axis. As shown in Fig. 2, the sample contains multiple domains, i.e., gyroid patches with different crystallographic directions relative to the same reference point. In Fig. 2b from top to bottom we see a transition from a well-oriented to an irregular region, which can be interpreted as the domain wall of the gyroid structure.

III. EXPERIMENT

To obtain a magnetic characterization of a 600 nm thick Ni gyroid sample, we perform ferromagnetic resonance (FMR) measurements [60] over a wide range of microwave frequencies. Using a vector network analyzer (VNA), we employ a broadband microwave signal generator and a

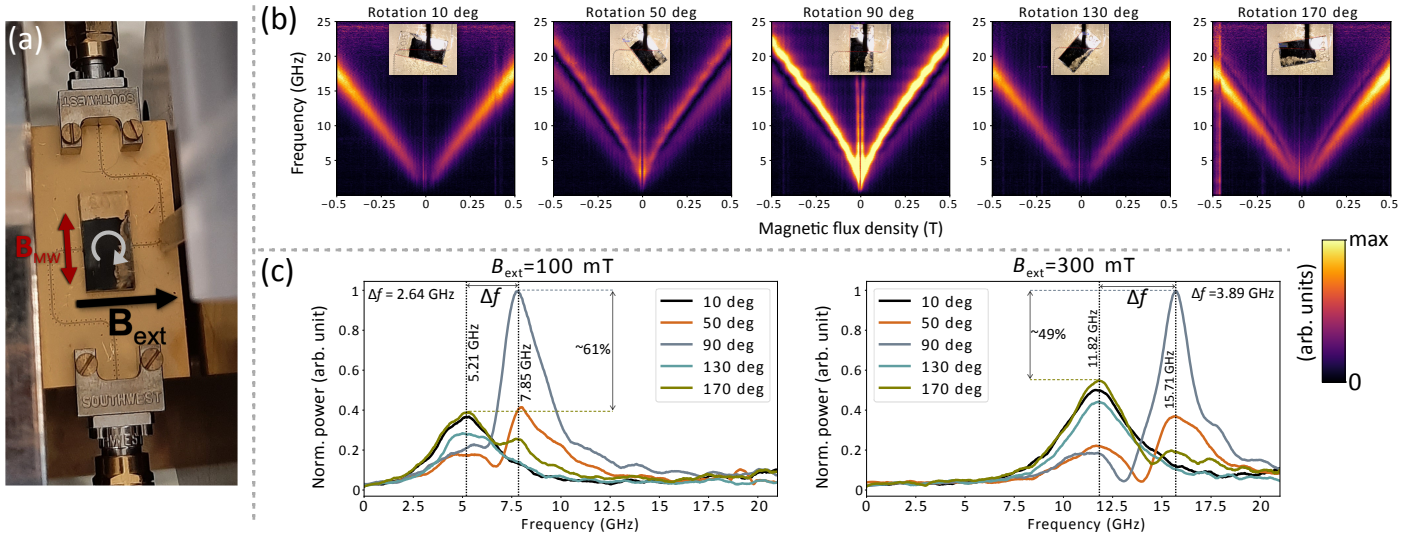

Figure 3. BBFMR measurement of the gyroid structure. The sample was rotated 180 deg relative to the CPW in 10 deg steps. For each configuration, a separate measurement of the energy absorption from the microwave field B_{MW} applied perpendicular to the static external magnetic field was performed as shown in (a). Plots of the dynamic magnetization amplitude as a function of static magnetic flux density and frequency for selected angles are presented in (b). They show a clear and cyclic transition from the lower frequency branch (10 deg) to the higher one (90 deg). Finally, (c) illustrates the frequency spectra for $B_{\mathrm{ext}} = 100$ mT and $B_{\mathrm{ext}} = 300$ mT. The separation between the bands (Δf) are measured to be 2.64 GHz and 3.89 GHz, respectively, as the field increases. Unlike amplitude, Δf is independent of rotation angle.

coplanar waveguide (CPW). Their use allows for the characterization of transmitted and reflected signals going to and from a microwave device over a wide range of frequencies [61].

The gyroid probe was mounted on an 80 µm wide CPW, allowing broadband measurements [62], 0.01-70 GHz, of FMR signals in a swept static field up to ∼1.3 T. A series of measurements were made for many different angles of sample rotation with respect to the CPW line to investigate the magnetic properties of the gyroid with different crystallographic directions. Fig. 3b shows a series of dynamic magnetization intensity maps as a function of static magnetic flux density and frequency, from 10 deg to 170 deg, in 40 deg steps. These results allow a clear conclusion that the FMR signal is strictly dependent on the orientation of the sample relative to the CPW – there is a cyclic transition of the signal from the lower frequency branch (for 10 deg) to the higher one (for 90 deg). As can be seen in Fig. 3c, for a static magnetic field $B_{\mathrm{ext}} = 100$ mT, the lower frequencies are concentrated around the value of 5.21 GHz, while the higher frequencies are concentrated around 7.85 GHz. For the field $B_{\mathrm{ext}} = 300$ mT, these values are 11.82 GHz and 15.71 GHz, respectively. Therefore, we can see that the separation of these branches is constant for different configurations of sample rotation and depends only on the value of the magnetic field, where for $B_{\mathrm{ext}} = 100$ mT it is $\Delta f = 2.64$ GHz, and for 300 mT – $\Delta f = 3.89$ GHz. In the case of intensities, however, it is different – with a change in sample orientation, the relative difference between the peaks of the low and high frequency branches changes across the entire rotation spectrum, covering the range from virtually 100% to 61% for $B_{\mathrm{ext}} = 100$ mT and to 49% for $B_{\mathrm{ext}} = 300$ mT. It is also worth noting that the half-width of the intensity peaks is larger for the lower frequency branch than for the higher frequency one. Due to the symmetry breaking, chirality, and general geometric complexity of the gyroid network, it was expected that the resonant frequency of the sample would shift with its rotation. However, it should be noted that the sample used is multi-domain, and the output signal from the BBFMR will certainly come from each of these domains at a different level.

IV. MICROMAGNETIC SIMULATIONS

In order to interpret the experimental results and to gain a deeper insight into the physics of the occurring phenomena, we decided to perform micromagnetic simulations of gyroid systems. For this purpose, we used the *tetmag* software, which solves the magnetostatic open boundary problem in large-scale micromagnetic simulations using the well-established finite element method (FEM) formalism [63]. Periodic boundary conditions were not assumed in any of the simulations presented.

In addition to its complex internal geometric structure on the nanoscale, the sample in the experiment has, on a macroscopic scale, the geometric feature of being almost planar. With a lateral size of a few millimeters and a thickness in the sub-micron range, our gyroid samples can be regarded as variants of magnetic films, rather than bulk materials. Since it is reasonable to assume that both the gyroid-like nanostructure of the material and the macroscopic shape of the sample can affect the magnetic material properties, we first test whether a flat gyroid network displays macroscopic shape anisotropy.

To this end, we analyze a quasi-planar $8 \times 8 \times 2$ gyroid model (number of the unit cells along the x, y, and z, re-

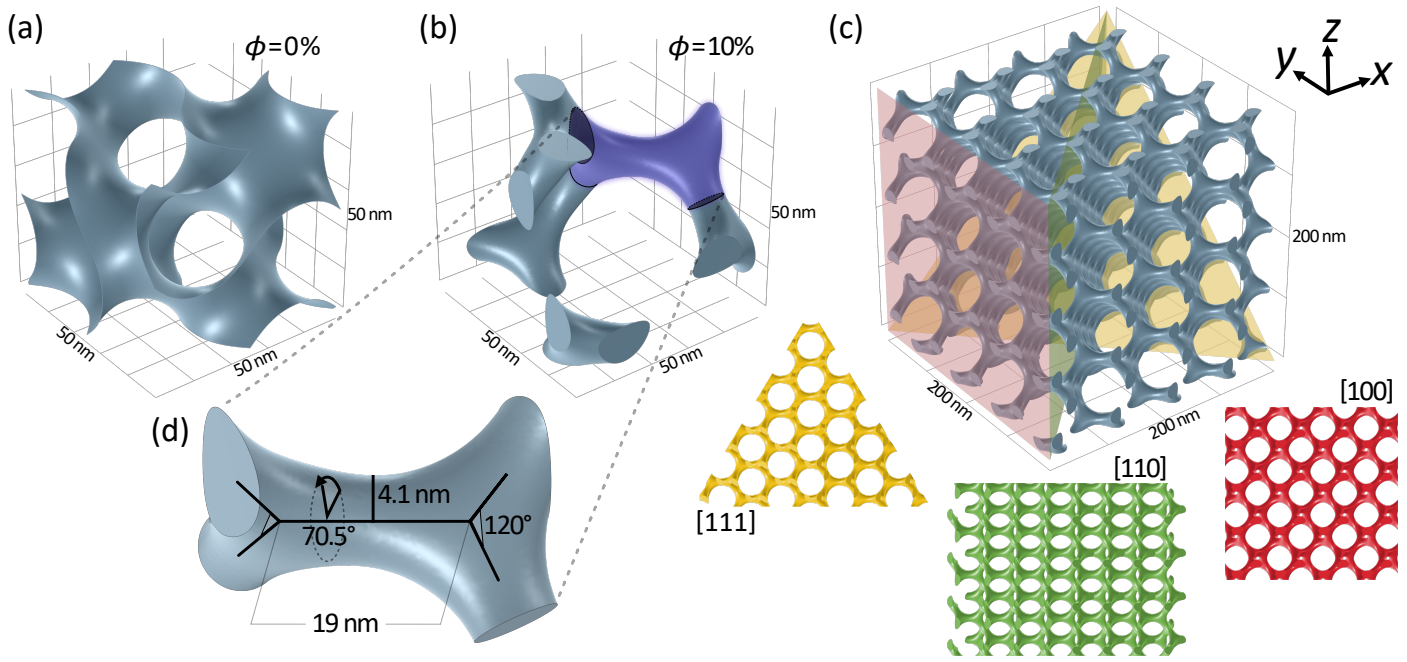

Figure 4. Structure of a 50 nm cubic gyroid unit cell with (a) volume fraction $\phi = 0\%$ and (b) $\phi = 10\%$, which is the subject of this study. To perform micromagnetic simulations, a geometric model (c) with $4 \times 4 \times 4$ unit cells ($200 \times 200 \times 200$ [nm]) was used. The three main high-symmetry directions of the gyroid network are shown below in the colors corresponding to the planes crossing the structure ([111] – yellow triangle, [110] – green rectangle, [100] – red square). Each shows the distribution and shape of channels characteristic of the gyroid, i.e. hexagonal pattern and round holes for [111], square pattern and elliptical holes for [110], and square pattern and round holes for [111]. In (d), an enlarged view of the chiral connection of two gyroid nodes is shown, together with the main geometric parameters of the system used in this research.

spectively) to verify the influence of shape anisotropy on resonant frequencies. The model here is $400 \times 400 \times 100$ nm in size (see Fig. 5) and consists of about 366 000 tetrahedral discretization cells. The geometric parameters of the gyroid unit cell are described in Fig. 4(b,d) and are the same for all models analyzed in this work. A filling fraction of 10% was assumed, which here corresponds to a cross-sectional radius of a single gyroid node of about 4.1 nm (where it is oval in shape) and an arm length of about 19 nm. The single unit cell of the structure has a dimension of 50 nm in each direction along [100] axes.

The following material parameters characteristic of thin Ni films were assumed, i.e. saturation magnetization $M_S = 480$ kA/m, exchange stiffness $A_{ex} = 8.6$ pJ/m, and g-factor equal to 2.14 [64, 65]. In each relaxation simulation, the Gilbert damping was set to a large value of $\alpha = 0.5$ to obtain a fast convergence to the equilibrium state. Then, for all frequency-domain simulations, this parameter was set to a low value of 0.01.

The low-amplitude alternating magnetic field applied in the frequency domain simulations generates a response of the magnetic system in the form of stationary magnetization oscillations with the frequency of the applied field. The magnetic susceptibility $\chi(\omega)$ describes the frequency-dependent relation between the externally applied oscillating field $\delta\mathbf{H}$ and the dynamic component of the magnetization $\delta\mathbf{M}$. For a more detailed discussion of the dynamic susceptibility and its definition see Ref. [66].

The susceptibility can be thought of as a complex quantity with a real and an imaginary component. In linear-response theory, the imaginary component of the susceptibility is related to dissipative processes in which the sample absorbs energy from the applied field. These absorption peaks denote resonances and generally coincide with frequencies of maximum oscillation amplitude of the dynamic magnetization. For the case of a spatially homogeneous harmonic magnetic field applied in the simulations, we can thus analyze the spatial distribution of the magnetization oscillation amplitude at these absorption peaks to identify the modes developing at these resonances. The colors in the mode visualizations (Figs. 5, 6 and 7) refer to the imaginary magnetic susceptibility component of the gyroid structure, which in this case is analogous to the modulus of the dynamic components of the magnetization.

The micromagnetic simulations are performed in two steps, where the first one is to calculate the stable (relaxed) magnetic configuration at a given field strength. After the magnetization relaxation, we performed simulations of the ferromagnetic resonance using a dedicated frequency domain algorithm [66]. We considered two cases where the external magnetic field is directed out-of-plane and in-plane – [100] and [001], respectively, which are crystallographically identical. We see in Fig. 5 an apparent anisotropy in the spectrum that changes in both field directions. The maximum absorption frequency shifts from about 8.25 GHz in the out-of-plane case to about 9.75 GHz in the in-plane scenario.

It can therefore be concluded that, when simulating mostly isotropic models of gyroid structures, such as the cubic structure shown in Fig. 1, we can expect resonant frequencies with values lower than those obtained from BBFMR measurements, due to the significant influence of

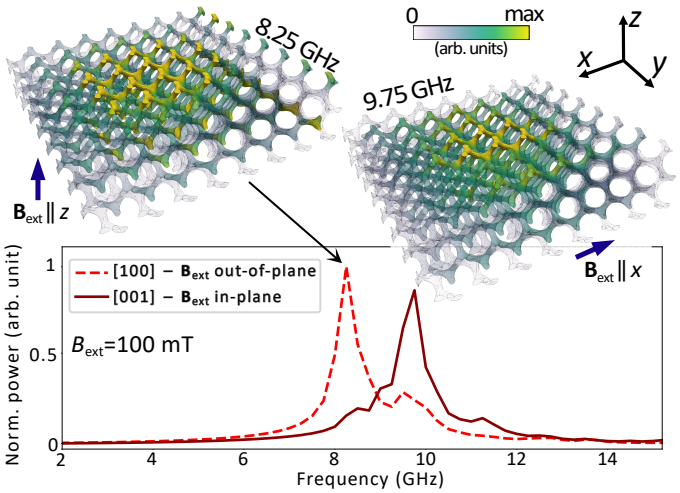

Figure 5. The resonance frequency spectra of $8 \times 8 \times 2$ gyroid samples obtained from micromagnetic simulations. The dashed line represents the signal of the sample magnetized with a 100 mT field directed out-of-plane (along the z-axis), while the solid line indicates the output of the sample magnetized in-plane (x-axis). The color scale corresponds to the imaginary part of the magnetic susceptibility.

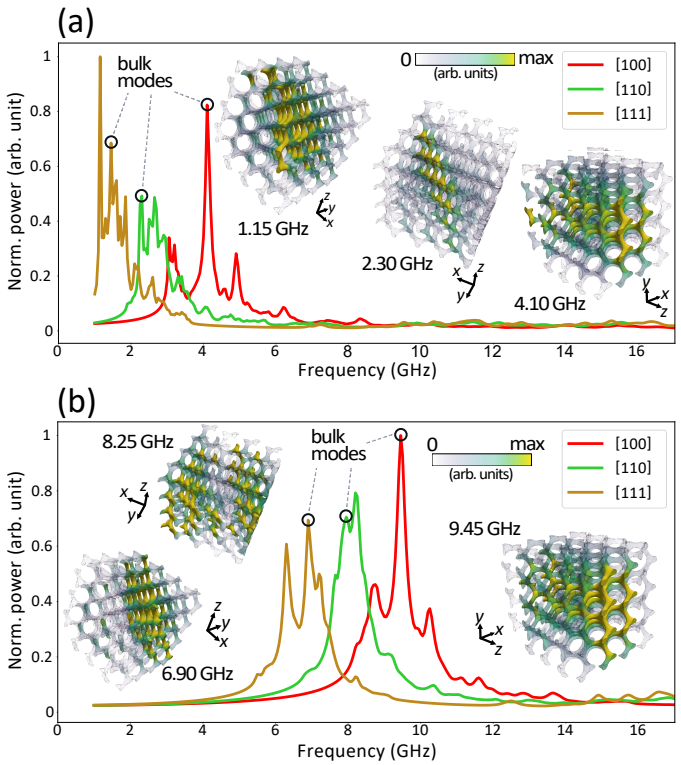

Figure 6. The resonance frequency spectra of $4 \times 4 \times 4$ gyroid samples obtained as a result of micromagnetic simulations. In (a) an external magnetic field of 100 mT is used, while in (b) it is 300 mT. In each plot, different colors indicate the crystallographic direction along which the field is applied, while the points marked with circles on the graph indicate the volumetric ferromagnetic resonance. In order of appearance, visualizations and values of the resonance frequencies are visible as insets to the plots. The color scale corresponds to the imaginary part of the magnetic susceptibility.

macroscopic shape anisotropy. The most accurate results of micromagnetic simulations could be obtained by simulating a much larger structure. However, due to limited computational resources and simulation time, it was necessary to limit the simulation to the dimensions under investigation. Nevertheless, in order to make a qualitative comparison with the experiment and to analyze the distribution of magnetization modes, it can be seen from the results in Fig. 3c and Fig. 5 that they are satisfactory for our purposes. The maximum intensity from the experiment for $B_{\text{ext}} = 300$ mT for certain rotation angles is at 11.5 GHz, while in the simulation at 9.75 GHz.

To qualitatively confirm the modulation and intensity shift of the FMR signal observed in the experiment during rotation of the gyroid sample and to study the effects at the nanometer scale, a gyroid model with dimensions of $4 \times 4 \times 4$ unit cells ($200 \times 200 \times 200$ nm, see Fig. 4c) was used in the second stage of micromagnetic simulations, consisting of about 630 000 tetrahedral discretization cells. The cubic shape of the structure allows a more accurate analysis of the dynamic magnetization distribution and insight into the effects associated with gyroid crystallography. The material parameters remain the same as for the $8 \times 8 \times 2$ structure.

Here we consider the three crystallographic directions [100], [110], and [111] (see Fig. 4c), and two different values of the external static magnetic field B_{ext} equal to 100 mT and 300 mT, as shown in Fig. 6. The time and computational resources required to simulate such complex structures dictate the limited choice of variables. At the same time, they allow us to obtain the necessary information about the ferromagnetic response of the gyroid system, which can be extrapolated qualitatively for various angles and external magnetic field values. The three crystallographic directions define this structure and rotationally induced differences in resonant frequencies are expected to be most pronounced for fields applied along them.

As can be seen in Fig. 6, the results of magnetic resonance simulations for gyroid structures reveal their strong geometric anisotropy. The graphs show the ferromagnetic response of a system with exactly $4 \times 4 \times 4$ unit cells. Therefore, only the resonant modes associated with the volumetric part of the structure were extracted for the analysis, ignoring the visible satellite peaks associated with the edge modes. If we compare the plots for the planar structure with Fig. 5, we see that in Fig. 6 the spectra are much richer for both values of the external magnetic field. This is due to the significantly larger contribution of edge modes to the overall signal in the case of cubic structures. Visualizations of these can be found in the Supporting Information. In the experiment, the structure of the gyroid is much larger than that analyzed here, so the manual selection of resonant modes was necessary. By selecting and visualizing the volumetric modes, we see that they arise in the inner part of the structure; therefore, they are the result of the gyroid geometry and not of the edges and artifacts created in the cutting area.

The results obtained from the resonance spectra support the experimental observations, especially in spite of the multi-domain nature of the sample used and its planar shape described above. They show qualitatively that the al-

ternation of resonance signals in the rotating gyroid sample in BBFMR can be clearly attributed to the crystallography-based anisotropy seen in the plots in Fig. 6. Comparing the plots for 100 mT in Fig. 6a and 300 mT in Fig. 6b, we see an apparent increase in frequencies. In contrast, the sequence and spacing of the resonance frequency peaks remain constant and equal to about 2.6 GHz between the two most distant bulk modes. This shows that the separation is strictly related to the geometry of the gyroid and can be predicted and tuned by changing the system parameters.

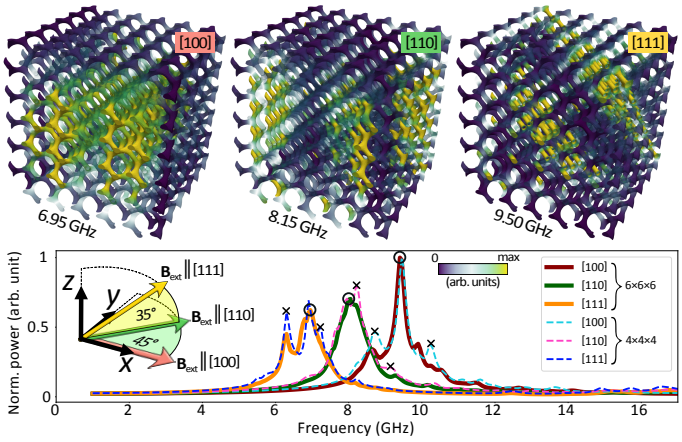

Figure 7. Spectral analysis of high-intensity volume modes of $6\times6\times6$ gyroid structures. In the lower part is a plot of the frequency spectra, where black circles indicate the volume modes shown in the upper part. In addition, spectra for smaller structures (dotted lines) have been plotted on the graph, showing a decrease in the intensity of the edge modes (marked with crosses) with increasing structure dimensions. The color scale on the mode visualizations corresponds to the imaginary part of the magnetic susceptibility.

In the final phase of the simulations, we decided to analyze an even larger, cubic structure of the gyroid to confirm the edge nature of the satellite peaks (which should have a lower relative intensity for such a structure) and to look at an additional effect initially observed in smaller systems. By visualizing the modes using micromagnetic simulations (Fig. 6), we discovered that there is an interesting localization of the high-amplitude magnetization precession. Therefore, we simulated and analyzed a $6\times6\times6$ unit cell gyroid structure discretized into more than 235 000 finite elements. This was done to improve the visibility of these modes relative to smaller structures and, to some extent, to enhance the signal of volume modes relative to satellite ones. The results in Fig. 7 (top row) show the magnetization intensity distribution clearly forming planes perpendicular to the 300 mT external magnetic field axis for the modes at 6.95 GHz for [100], 8.15 GHz for [110] and 9.50 GHz for [111]. Moreover, in the case of the field directed along [100] and [110], the modes appear to be periodic, which was not evident in the $4\times4\times4$ structure. The graph at the bottom of Fig. 7 shows the FMR spectrum resulting from simulations of the $6\times6\times6$ model for the three crystallographic directions studied. For comparison with analogous calculations for a smaller structure (Fig. 6b), the results of these simulations have been overlaid on the graph as dashed lines. It can be seen that the influence of edge modes (marked with a cross) decreases as expected with increasing model dimensions, while the normalized intensity of volume modes (marked with a circle) remains constant.

V. DISCUSSION

One of the realized goals of the micromagnetic simulations was to reproduce the observations from the BBFMR experiment, where we detected the alternate appearance of two separate signals for different sample rotation angles. Due to the multi-domain structure of the sample, it is difficult to define a dominant crystallography and thus its direct quantitative effect on the resonance spectrum. Therefore, in this paper we have numerically tested the three selected field directions ([100], [110] and [111]) to see if the complexity, chiral properties and curvature of the gyroid affect the change in resonance frequency in a similar and analogous manner to the experimental observations. Obviously, in addition to the shape anisotropy, analyzed in the $8\times8\times2$ case, there are many other aspects that cannot be predicted in the fabrication of such complex structure, and thus cannot be applied in the simulation, such as irregularities and impurities in the shape and/or thickness of the nanorods, and lack of information about the sample's dominant crystallographic direction in each experimental configuration. All this potentially contributes to the discrepancy between the simulation and the experimental frequency shift due to the change in the angle of the incident field, which, despite the assumption of an ideal gyroid model, is only about 1.75 GHz, roughly 15% of the measured signal in BBFMR.

The micromagnetic simulations also show that the gyroidal geometry exhibits specific mode-bounding properties that cause the magnetization distribution to form layered patterns whose spacing depends on the system parameters. Such a metamaterial-like behavior is promising for the application of 3D gyroidal structures in various types of magnonic probes where, knowing the localization period, one could obtain information about much smaller internal dimensions of the structure.

VI. CONCLUSIONS

In this work, ferromagnetic resonance analysis of three-dimensional gyroidal Ni nanostructures was performed. Experimental measurements were conducted using BBFMR, in which a multi-domain gyroid sample was rotated relative to the CPW line, to study the ferromagnetic response of the system for different angles of incidence of both static and dynamic magnetic fields. The measurements were supported by FEM micromagnetic simulations in the *tetmag* software, the aim of which was to interpret the experimental results and to gain insight into the magnetization distribution in the gyroid nanostructure. We quantified the FMR results by first numerically analyzing the $8\times8\times2$ unit cell to approximate the planar sample used in the BBFMR measurements, and then performed simulations for cubic-like $4\times4\times4$ and $6\times6\times6$ structures for 100 mT and 300 mT rotating external magnetic field.

The key finding from our simulations is the significant

role of the crystallographic orientation of the gyroid with respect to the incident magnetic field. The results provide insight into the properties of three-dimensional gyroid structures, which are a fascinating topic in magnonics and spintronics due to their unique chiral geometry and curvature. The strong influence of the magnetic field direction on the resonant frequencies was demonstrated experimentally and theoretically, revealing its stronger and weaker coupling for individual crystallographic directions (amplitude modulation in BBFMR), and qualitatively confirmed by micromagnetic simulations. They also revealed the topological-like property of this structure that forces the resonance modes to periodically concentrate plane-wise, perpendicular to the direction of the static magnetic field. These discoveries have significant potential applications in the development of 3D magnonics, where gyroid structures could become a fundamental building block.

ACKNOWLEDGMENTS

The research leading to these results was funded by the National Science Centre of Poland, Project No. UMO-2020/39/I/ST3/02413. J.L. and S.F. acknowledge support from the Japan Society for the Promotion of Science (JSPS) under KAKENHI 21K04816 and 19H05622, Cooperative Research Projects of CSIS, Tohoku University, and the Graduate Program for Spintronics (GP-Spin), Tohoku University. R.H. acknowledges the High Performance Computing center of the University of Strasbourg for supporting this work by providing access to computing resources.

[1] P. Pirro, V. I. Vasyuchka, A. A. Serga, and B. Hillebrands, Nature Reviews Materials **6**, 1114 (2021).
[2] A. A. Serga, A. V. Chumak, and B. Hillebrands, Journal of Physics D: Applied Physics **43**, 264002 (2010).
[3] P. Yan and G. E. Bauer, IEEE Transactions on Magnetics **49**, 3109 (2013).
[4] J. Barker and G. E. Bauer, Physical Review Letters **117**, 217201 (2016).
[5] F. Garcia-Sanchez, P. Borys, R. Soucaille, J. P. Adam, R. L. Stamps, and J. V. Kim, Physical Review Letters **114**, 247206 (2015).
[6] K. Wagner, A. Kákay, K. Schultheiss, A. Henschke, T. Sebastian, and H. Schultheiss, Nature Nanotechnology **11**, 432 (2016).
[7] G. Duerr, K. Thurner, J. Topp, R. Huber, and D. Grundler, Physical Review Letters **108**, 227202 (2012).
[8] J. Lan, W. Yu, R. Wu, and J. Xiao, Physical Review X **5**, 041049 (2015).
[9] A. V. Chumak, V. I. Vasyuchka, A. A. Serga, and B. Hillebrands, Nature Physics **11**, 453 (2015).
[10] V. V. Kruglyak, S. O. Demokritov, and D. Grundler, Journal of Physics D: Applied Physics **43**, 264001 (2010).
[11] B. Lenk, H. Ulrichs, F. Garbs, and M. Münzenberg, Physics Reports **507**, 107 (2011).
[12] A. Barman *et al.*, Journal of Physics Condensed Matter **33**, 413001 (2021).
[13] A. V. Chumak *et al.*, IEEE Transactions on Magnetics **58**, 1 (2022).
[14] G. Gubbiotti, *Three-Dimensional Magnonics*, 1st ed., edited by G. Gubbiotti (Jenny Stanford Publishing, New York, 2019).
[15] R. Hertel and R. Cheenikundil, doi.org/10.21203/rs.3.rs-846190/v1 (2022).
[16] P. Fischer, D. Sanz-Hernández, R. Streubel, and A. Fernández-Pacheco, APL Materials **8**, 010701 (2020).
[17] D. Makarov, O. M. Volkov, A. Kákay, O. V. Pylypovskyi, B. Budinská, and O. V. Dobrovolskiy, Advanced Materials **34**, 2101758 (2022).
[18] R. Cheenikundil, J. Bauer, M. Goharyan, M. D'Aquino, and R. Hertel, APL Materials **10**, 81106 (2022).
[19] J. Llandro, D. M. Love, A. Kovács, J. Caron, K. N. Vyas, A. Kákay, R. Salikhov, K. Lenz, J. Fassbender, M. R. Scherer, C. Cimorra, U. Steiner, C. H. Barnes, R. E. Dunin-Borkowski, S. Fukami, and H. Ohno, Nano Letters **20**, 3642 (2020).
[20] A. Fernández-Pacheco, R. Streubel, O. Fruchart, R. Hertel, P. Fischer, and R. P. Cowburn, Nature Communications **8**, 1 (2017).
[21] C. Donnelly, A. Hierro-Rodríguez, C. Abert, K. Witte, L. Skoric, D. Sanz-Hernández, S. Finizio, F. Meng, S. McVitie, J. Raabe, D. Suess, R. Cowburn, and A. Fernández-Pacheco, Nature Nanotechnology **17**, 136 (2022).
[22] M. Hunt, M. Taverne, J. Askey, A. May, A. Van Den Berg, Y. L. D. Ho, J. Rarity, and S. Ladak, Materials **13**, 761 (2020).
[23] A. van den Berg, M. Caruel, M. Hunt, and S. Ladak, Nano Research **16**, 1441 (2023).
[24] A. H. Schoen, *Infinite periodic minimal surfaces without self-intersections*, Tech. Rep. (NASA Electronics Research Center, Cambridge, 1970).
[25] C. A. Lambert, L. H. Radzilowski, and E. L. Thomas, Philosophical Transactions of the Royal Society A: Mathematical, Physical and Engineering Sciences **354**, 2009 (1996).
[26] M. D. Turner, M. Saba, Q. Zhang, B. P. Cumming, G. E. Schröder-Turk, and M. Gu, Nature Photonics **7**, 801 (2013).
[27] S. Vignolini, N. A. Yufa, P. S. Cunha, S. Guldin, I. Rushkin, M. Stefik, K. Hur, U. Wiesner, J. J. Baumberg, and U. Steiner, Advanced Materials **24**, OP23 (2012).
[28] J. A. Dolan, B. D. Wilts, S. Vignolini, J. J. Baumberg, U. Steiner, and T. D. Wilkinson, Advanced Optical Materials **3**, 12 (2015).
[29] P. Farah, A. Demetriadou, S. Salvatore, S. Vignolini, M. Stefik, U. Wiesner, O. Hess, U. Steiner, V. K. Valev, and J. J. Baumberg, Physical Review Applied **2**, 044002 (2014).
[30] K. Michielsen and D. G. Stavenga, Journal of the Royal Society Interface **5**, 85 (2008).
[31] K. Michielsen, H. De Raedt, and D. G. Stavenga, Journal of the Royal Society Interface **7**, 765 (2010).
[32] V. Saranathan, C. O. Osuji, S. G. Mochrie, H. Noh, S. Narayanan, A. Sandy, E. R. Dufresne, and R. O. Prum, Proceedings of the National Academy of Sciences of the United States of America **107**, 11676 (2010).
[33] G. E. Schröder-Turk, S. Wickham, H. Averdunk, F. Brink, J. D. Fitz Gerald, L. Poladian, M. C. Large, and S. T. Hyde, Journal of Structural Biology **174**, 290 (2011).
[34] T. B. Schroeder, J. Houghtaling, B. D. Wilts, and M. Mayer, Advanced Materials **30**, 1705322 (2018).
[35] C. Yan, L. Hao, A. Hussein, and D. Raymont, International Journal of Machine Tools and Manufacture **62**, 32 (2012).

[36] A. Yánez, A. Herrera, O. Martel, D. Monopoli, and H. Afonso, Materials Science and Engineering C **68**, 445 (2016).

[37] Z. Gan, M. D. Turner, and M. Gu, Science Advances **2**, e1600084 (2016).

[38] G. S. Armatas and M. G. Kanatzidis, Nature **441**, 1122 (2006).

[39] C. T. Kresge, M. E. Leonowicz, W. J. Roth, J. C. Vartuli, and J. S. Beck, Nature **359**, 710 (1992).

[40] D. A. Hajduk, P. E. Harper, S. M. Gruner, C. C. Honeker, G. Kim, L. J. Fetters, and G. Kim, Macromolecules **27**, 4063 (1994).

[41] J. K. Kim, S. Y. Yang, Y. Lee, and Y. Kim, Progress in Polymer Science (Oxford) **35**, 1325 (2010).

[42] W. Bai, A. F. Hannon, K. W. Gotrik, H. K. Choi, K. Aissou, G. Liontos, K. Ntetsikas, A. Alexander-Katz, A. Avgeropoulos, and C. A. Ross, Macromolecules **47**, 6000 (2014).

[43] H. Y. Hsueh, C. T. Yao, and R. M. Ho, Chemical Society Reviews **44**, 1974 (2015).

[44] L. V. Lich, D. T. H. Hue, D. T. H. Giang, N. H. Duc, T. Shimada, T. Kitamura, and V. H. Dinh, Acta Materialia **249**, 118802 (2023).

[45] R. Hertel, SPIN **03**, 1340009 (2013), publisher: World Scientific Publishing Co.

[46] Y. Gaididei, V. P. Kravchuk, and D. D. Sheka, Physical Review Letters **112**, 257203 (2014), publisher: American Physical Society.

[47] R. Streubel, P. Fischer, F. Kronast, V. P. Kravchuk, D. D. Sheka, Y. Gaididei, O. G. Schmidt, and D. Makarov, Journal of Physics D: Applied Physics **49**, 363001 (2016).

[48] D. Sander, S. O. Valenzuela, D. Makarov, C. H. Marrows, E. E. Fullerton, P. Fischer, J. McCord, P. Vavassori, S. Mangin, P. Pirro, B. Hillebrands, A. D. Kent, T. Jungwirth, O. Gutfleisch, C. G. Kim, and A. Berger, Journal of Physics D: Applied Physics **50**, 363001 (2017).

[49] D. D. Sheka, Applied Physics Letters **118**, 230502 (2021).

[50] R. Shindou, R. Matsumoto, S. Murakami, and J. I. Ohe, Physical Review B - Condensed Matter and Materials Physics **87**, 174427 (2013).

[51] P. A. McClarty, Annual Review of Condensed Matter Physics **13**, 171 (2022).

[52] O. M. Volkov, U. K. Rößler, J. Fassbender, and D. Makarov, Journal of Physics D: Applied Physics **52**, 345001 (2019).

[53] J. J. Hopfield, Proceedings of the National Academy of Sciences of the United States of America **79**, 2554 (1982).

[54] H. Karcher, Manuscripta Mathematica **64**, 291 (1989).

[55] K. Große-Brauckmann and M. Wohlgemuth, Calculus of Variations and Partial Differential Equations **4**, 499 (1996).

[56] K. Große-Brauckmann, Experimental Mathematics **6**, 33 (1997).

[57] T. Sunada, Notices of the AMS **55**, 208 (2008).

[58] S. T. Hyde, M. O'Keeffe, and D. M. Proserpio, Angewandte Chemie - International Edition **47**, 7996 (2008).

[59] A. Mizuno, Y. Shuku, and K. Awaga, Bulletin of the Chemical Society of Japan **92**, 1068 (2019).

[60] B. Heinrich, in *Ultrathin Magnetic Structures II*, edited by B. Heinrich and J. Bland (Springer, Berlin, Heidelberg, 1994) pp. 195–296.

[61] E. Montoya, T. McKinnon, A. Zamani, E. Girt, and B. Heinrich, Journal of Magnetism and Magnetic Materials **356**, 12 (2014).

[62] J. Dubowik and H. Głowiński, Current Topics in Biophysics **33**, 43 (2010).

[63] R. Hertel, S. Christophersen, and S. Börm, Journal of Magnetism and Magnetic Materials **477**, 118 (2019).

[64] J. M. Coey, *Magnetism and Magnetic Materials* (Cambridge University Press, 2010) pp. 1–617.

[65] M. Singh, J. Callaway, and C. S. Wang, Physical Review B **14**, 1214 (1976).

[66] M. D'Aquino and R. Hertel, Journal of Applied Physics **133**, 033902 (2023).